Modeling of Spray Pyrolysis-Why are the Synthesized Y2O3 Microparticles Hollow?

Nicolas Reuge, Brigitte Caussat, Nicolas Joffin, Jeannette Dexpert-Ghys, Marc Verelst, Henri Dexpert

Modeling of Spray Pyrolysis—Why are the Synthesized Y_2O_3 Microparticles Hollow?

N. Reuge and B. Caussat
Laboratoire de Génie Chimique/ENSIACET/INPT, UMR CNRS 5503, 5 Rue Paulin Talabot, BP1301, 31106 Toulouse Cedex 1, France

N. Joffin, J. Dexpert-ghys, M. Verelst, and H. Dexpert
CEMES, UPR CNRS 8011, 29 Rue Jeanne Marvig, 31055 Toulouse Cedex, France

There are some major advantages to be gained in processing micronic europium doped yttrium oxide Y_2O_3 particles for phosphor applications using spray pyrolysis. To better understand the influence of the operating conditions and also why hollow particles are formed, a complete one-dimensional modeling of the pure evaporation then evaporation/precipitation steps of micronic water/$Y(NO_3)_3$ droplets has been performed. Among the main results, it appears that no concentration gradient exists inside droplets during the pure evaporation stage and that the evaporation/precipitation stage, occurring in less than 10^{-3} s, leads to compact particles theoretically formed of a coherent porous medium of $Y(NO_3)_3{\cdot}5H_2O$. But the analysis of phenomena occurring during the thermolysis step between 95 and 300°C has revealed that a partial liquefaction of the hydrated yttrium nitrate occurs with concomitant release of gas. As a consequence, a crust of lightly hydrated yttrium nitrate probably appears, followed by particle inflation and leading to the formation of broken hollow particles.

Keywords: spray pyrolysis, evaporation, precipitation, micronic particles, yttrium nitrate

Introduction

Spray pyrolysis (SP) is an aerosol process commonly used to produce a wide variety of materials in powder form[1,2] including metals, metal oxides, ceramics, superconductors, fullerenes, and nanostructured materials. The sizes of the processed particles are most often micronic and submicronic (50 nm to 5 μm). This technology has been used for many years in the material, chemical, and food industries. There are five main steps: (i) generation of a spray from a liquid precursor by an appropriate droplet generator, (ii) spray transport by air flow during which solvent evaporation occurs then concomitant solute precipitation when the critical supersaturation limit is exceeded in the droplets, (iii) thermolysis of the precipitated particles at higher temperatures to form micro/nanoporous particles, (iv) intraparticle sintering to form dense particles, (v) finally, extraction of the particles from the gas flow. SP offers specific advantages over conventional material processing techniques[1,2] (gas-to-particle conversion processes, liquid or solid-state processing followed by milling), such as a higher purity of the powders produced, a more uniform chemical composition, a narrower size distribution, a better regularity in shape, and the synthesis of multicomponent materials. Another advantage is the relative simplicity of the process which allows easy scale-up.[3]

However, challenges still exist for SP, e.g. to increase production rates, to better understand the influence of the operating conditions, to control the particle size,[4] shape and inter-

Correspondence concerning this article should be addressed to B. Caussat at brigitte.caussat@ensiacet.fr.

nal morphology. Three main types of particle morphology can be obtained: (i) completely filled or "solid" nanoporous particles, (ii) microporous particles, and (iii) hollow (shell-like) particles. For instance, Lyons et al.[5] obtained hollow MgO and ZnO particles and full Al_2O_3 particles from nitrate salt precursors. No change in particle size or morphology was observed in nitrate-derived ZnO or MgO by modifying the initial air humidity or the heating rate. The addition of small amounts of seed particles with or without (i) an initial saturated drying environment and (ii) temperature gradient modifications in the flow system also had no effect. However, Lenggoro et al.[6] observed a radical change in the morphology of ZrO_2 particles with a diameter of about 3 μm, from hollow to completely filled spheres, by changing the process temperature.

Over the past years, our group has performed many SP syntheses on a large variety of materials. Y_2O_3 (this work), Y_2O_3:Eu, ZrO_2, and CeO_2 syntheses, from nitrate precursors, lead to hollow spheres[7] whereas Zn_2SiO_4 and ZnO syntheses from zinc nitrate lead to microporous spheres.[8] We never have been able to significantly modify the initial hollow/filled morphology given by a specific precursor by changing the heat, flow, or concentration conditions during the evaporation, precipitation, or thermolysis steps. However, it has been shown that adding polymeric constituents such as polyethylene glycol[9–11] to the solution could lead to well controlled solid particle morphology.

The origin of the hollowness of the particles is not certain and does not seem to be always the same, but the most often mentioned mechanism is the formation of large solute concentration gradients in the droplets, leading to precipitation only at their surface.[1,2] Several modeling works have been performed to progress in the understanding of the phenomena involved. Jayanthi et al.[12] focused on modeling spray drying of an aqueous solution of zirconyl hydroxide chloride. They concluded that volume precipitation into droplets is favored by a very gradual increase of the spray temperature along the reactor, high initial solute concentrations, small initial droplet diameters, a high number density of droplets, and a weak flow rate of the carrier gas. Moreover, solutes presenting large differences between their saturation and their supersaturation concentrations promote volume precipitation and thus should be preferred. Yu and Liao[13] studied the drying of millimetric water droplets containing sodium chloride. Their results agree with those of Jayanthi et al., but they claim that a small initial concentration of solute seems to promote the formation of filled particles. Xiong and Kodas[14] also simulated the drying of water/NaCl droplets, but of micronic sizes. In almost all the operating conditions tested, they find that no solute concentration gradient occurred.

Another point must be emphasized: as reported by Messing et al.[11] and by Gurav et al.,[1] the thermal properties of the precipitated precursor can impact on subsequent particle evolution during the thermolysis stage. For example, many metal nitrates have low melting temperatures (e.g. $< 200^{\circ}C$). If the metal salt melts during thermolysis, its permeability decreases and the gas released is trapped inside the particle. An increase of the internal gas pressure may then result in the "explosion" or foaming of the particle. This process could lead to hollow particles or particle fragments. Charlesworth and Marshall[15] proposed a similar explanation: when the boiling temperature of the remaining solvent is exceeded, thermoplastic salts readily inflate, whereas impermeable, rigid particles simply fracture into shell fragments. Lin and Gentry[16] validated these explanations experimentally for millimetric droplets with various precursors and developed interesting modeling studies.[17–19] In Reuge and Caussat,[20] a general dimensionless study of the evaporation and precipitation stages of SP allowed to determine, whatever the diluted salt, the conditions that must be fulfilled to obtain hollow particles. We also showed that no formation of solute concentration gradients does not necessary lead to the synthesis of solid particles and that conversely the formation of solute concentration gradients does not necessary lead to the synthesis of hollow particles.

Europium-doped yttrium oxide (Y_2O_3:Eu) was discovered decades ago but is still considered to be one of the best red inorganic phosphors, due to the sharp emission ($\lambda = 611$ nm) of the europium ion activator (Eu^{3+}) in the host lattice (Y_2O_3), its excellent luminescence efficiency, color purity, and stability.[21] SP is one efficient alternative process for its large scale production.[3,22] Micronic particles of Y_2O_3:Eu synthesized by SP are hollow spheres. They exhibit the required luminescence efficiency for plasma display panel applications (under vacuum ultraviolet excitation), but the core-shell morphology is unfavorable for applications requiring near ultraviolet excitation.[7,8]

A pilot-scale SP set-up has been assembled in our laboratory and tested using yttrium nitrate precursor, europium was not introduced here for cost considerations. Since the physical chemical properties of Y and Eu are very close and because the molar doping level in the red phosphor is low (1Eu/19Y), we can assume that the results of experiments and modeling using pure Y_2O_3 are also valid for the red phosphor. The aim of the present work is to understand the processes leading to the hollow morphology of the particles and the influence of the main operating conditions. For these purposes, the first modeling study of SP using yttrium nitrate as a precursor salt has been performed. A 1D modeling study of the pure evaporation step then of the evaporation/precipitation stage will be detailed. Phenomena will be investigated at the scale of the drying column and at the scale of the individual droplet. Different scenarios will be proposed to represent the evaporation/precipitation stage. The influence of the main operating parameters on the process behavior will be numerically studied. Finally, phenomena occurring during the thermolysis step will be discussed on the basis of theoretical and experimental data. For all the physical steps considered, those mechanisms that could be at the origin of the particle hollowness will be analyzed.

Process Description and Operating Conditions

An ultrasonic generator (ARECO/ARIV), working at 1.6 MHz generated micronic droplets from $Y(NO_3)_3$ diluted in water at 0.6 mol/l. The droplets were transported by an air flow through successively:

- a vertical drying column: 20 cm internal diameter, 1.8 m long,
- then a horizontal decomposition/densification column: 20 cm internal diameter, 1.8 m long.

The heating system was juxtaposed electrical furnaces of 12 kW total power. Thermocouples on the outer wall of the reactor allowed the temperature to be adjusted up to 250°C in the drying zone and up to 1000°C in the decomposition/densification zone. The solid phase was then separated from the vapor phase in a bag filter.

For the experiments described here, the inlet spray temperature was 31°C, and the outer wall temperature of the drying zone was fixed to 225°C. The inner wall temperature profiles have been measured and found to vary from 31 to 205°C along the column height.

Four air flow rates have been considered: 2.7, 4.7, 5.7, and 8.7 m^3/h STP. The ultrasonic droplet generator delivers solution flow rates proportional to air flows and respectively equal to 0.32, 0.55, 0.67, and 1 l/h STP.

Droplet diameter distributions were measured with a Spraytech™ Malvern laser size analyzer positioned at the drying column inlet. A mean droplet radius R_0 of 2.9 μm was considered in all cases and the number droplet concentration was about 1.2×10^6 cm^{-3}.

It must be emphasized that preliminary calculations have shown that, over the whole range of operating parameters, the evaporation process is extremely intense at ambient temperature as long as the air is not completely saturated with water vapor at the droplet surface (i.e. the interfacial relative humidity is equal to 100%). Since, of course, this fast evaporation occurs between the nebulization area and the reactor inlet, air is already completely saturated with water vapor at the droplet surface at the reactor inlet and the solute concentration in the droplets is no longer 0.6 mol/l, but 0.75 mol/l. The specific humidity of air Y_0 at the inlet was therefore 0.026.

The powders were characterized by TGA/TDA analysis with a SETARAM Labsys, and by XRD on a Seifert XRD 3000 diffractometer. The powder microsructure was observed by transmision electron microscopy (TEM) on a Philips CM12 and by scanning electron microcopy (SEM) on a Jeol 6700F.

Modeling the Pure Evaporation Stage

Assumptions, equations, and physical properties of the fluids

A 1D model at the scale of the column and a 0D model at the scale of the droplet were developed first. The following assumptions were retained:

(i) gas flow is laminar since the Reynolds number varies between 300 and 1000,

(ii) all parameters are uniform inside droplet,

(iii) at the column scale, momentum, heat and mass transfer phenomena in the radial direction can be ignored (note that the mean radial temperature gradient was 3.5°C/cm and only 1.2°C/cm between a radial position of 2.5 cm from the wall and the center of the column),

(iv) the heat flux density q through the column walls is proportional to the difference between the inner wall and gas temperatures:

$$q = \kappa(T_{\text{wall}} - T_{\text{gas}}) \tag{1}$$

Values of constant κ were fixed such that the calculated temperatures fit the average spray temperatures measured 1.5 m after the column inlet: 92, 90, 82, and 63°C for air flow rates of 2.7, 4.7, 5.7, and 8.7 m^3/h STP respectively,

(v) the relative velocity between droplets and carrier gas is zero and there is no interaction between droplets,

(vi) axial diffusion of water vapor in air is negligible,

(vii) the Kelvin effect is negligible because droplets remain much larger than 0.1 μm,

(viii) the solute begins to precipitate as soon as the saturation concentration is reached, the supersaturation concentration of yttrium nitrate in water being unknown.

The mean mass fractions of water inside droplets/particles and in air are given by the following dimensionless expressions:

$$\begin{cases} X = w_{\text{w}}^{\text{liq}}\left(w_{\text{s}}^{\text{liq}} + w_{\text{s}}^{\text{cryst}}\right)^{-1} \\ Y = w_{\text{w}}^{\text{vap}} w_{\text{a}}^{-1} \end{cases} \tag{2}$$

where w_{a} and $w_{\text{w}}^{\text{vap}}$ are the mass fractions of air/water vapor in the gas, $w_{\text{w}}^{\text{liq}}$ the mass fraction of liquid water in a droplet, and $w_{\text{s}}^{\text{liq}}$ the mass fraction of the solute in the droplet. Four equations must be solved: the mass conservation at the reactor scale (3) and at the droplet scale (4), the energy equation at the reactor scale (5), and at the droplet scale (6). Considering the assumptions previously detailed, they take the following form (note that parameter Z will be used for the evaporation/precipitation stage and must be taken here equal to zero):

$$\begin{cases} F_{\text{a}} Y + F_{\text{s}}(X+Z) = F_{\text{w}} & (3) \\ v_z m_{\text{s}} \frac{\partial (X+Z)}{\partial z} = -(4\pi R) D_{\text{v}} \rho_{\text{a}} \left(Y_{\text{int}}\left(T_{\text{gas}}/T_{\text{liq}}\right) - Y\right) & (4) \\ F_{\text{s}}(1+X+Z) C p_{\text{d}} \frac{\partial T_{\text{liq}}}{\partial z} + F_{\text{a}}\left(C p_{\text{a}} + Y C p_{\text{w}}^{\text{vap}}\right) \cdot \frac{\partial T_{\text{gas}}}{\partial z} - F_{\text{s}} h_{\text{vap}} \frac{\partial (X+Z)}{\partial z} & \\ \quad - F_{\text{s}} \Delta H (1 + Z_{\text{f}}^{-1}) \frac{\partial Z}{\partial z} - \frac{\partial}{\partial z}\left(\lambda_{\text{gas}} \frac{\partial T_{\text{gas}}}{\partial z}\right)\left(\pi R_{\text{c}}^2\right) = q\left(2\pi R_{\text{c}}\right) & (5) \\ v_z m_{\text{d}} C p_{\text{d}} \frac{\partial T_{\text{liq}}}{\partial z} = \left(4\pi R\right)\lambda_{\text{gas}}\left(T_{\text{gas}} - T_{\text{liq}}\right) + v_z m_{\text{s}} h_{\text{vap}} \frac{\partial (X+Z)}{\partial z} & \\ \quad + v_z m_{\text{s}} \Delta H \left(1 + Z_{\text{f}}^{-1}\right) \frac{\partial Z}{\partial z} & (6) \end{cases}$$

Table 1. Physical Properties of Water and Aqueous $Y(NO_3)_3$

Density (kg/m^3), from Rard[23]:

$$\rho_{liq}(25°C) = a_1 + a_2/X + a_3/X^{1.5} + a_4/X^2 + a_5/X^{2.5} + a_6/X^3 + a_7/X^{3.5} + a_8/X^4 + a_9/X^{4.5}$$

With: $a_1 = 995;\ a_2 = 0.8178;\ a_3 = 2.855 \times 10^{-2};\ a_4 = -0.8367;\ a_5 = 2.2764;\ a_6 = -4.1271;$
$a_7 = 3.9393;\ a_8 = -1.8699;\ a_9 = 0.3532$

Water activity, from Rard[23]:

$$a_w(25°C) = \exp\left[-4/X \cdot 18/275\left(1 - b_0/X^{0.5} + b_1/X^{0.75} + b_2/X + b_3/X^{1.25} + b_4/X^{1.5} + b_5/X^{1.75} + b_6/X^2 + b_7/X^{2.25}\right)\right]$$

With: $b_0 = 5.4939;\ b_1 = -7.8834;\ b_2 = 164.4546;\ b_3 = -555.8051;\ b_4 = 913.9005;$
$b_5 = -814.9047;\ b_6 = 378.477;\ b_7 = -71.97$

Water vapor saturation pressure in air (Pa), from Reid et al.[24]:

$$P_{sat} = \frac{10^5}{760} \exp\left(18.3036 - \frac{3816.44}{T_{liq} - 46.13}\right)$$

Mean ionic activity coefficient, from Rard[23]:

$$\gamma_{\pm}(25°C) = \exp\left(-3b_0/X^{0.5} + 2.333b_1/X^{0.75} + 2b_2/X + 1.8b_3/X^{1.25} + 1.666b_4/X^{1.5} + 1.5714b_5/X^{1.75} + 1.5b_6/X^2 + 1.444b_7/X^{2.25}\right)$$

(Same coefficients as a_w)

Solubility (g/100g of water) fitted from experimental results[25,26]:

$S = c_0 + c_1 T_{liq} + c_2 . \arctan(c_3 T_{liq} - c_4)$

With:

$c_0 = -150.3776;\ c_1 = 1.1185\ K^{-1};\ c_2 = 25.3241;\ c_3 = 0.1588\ K^{-1};\ c_4 = 54.5378$

where air, water, and solute flow rates F_a, F_w, and F_s are expressed in kg/s. The main physical properties of the fluids are given in Table 1.[23–26]

These equations have been successfully validated by Yu and Liao[13] from experimental investigations of evaporation of water/NaCl and water/NH_4NO_3 droplets performed by Ranz and Marshall.[27]

The reduced mass fraction of water Y_{int} at the liquid/gas interface at the saturation pressure is defined as:

$$Y_{int} = a_w M_w (M_a P_0)^{-1} P_{sat} \tag{7}$$

where a_w is the water activity, dependent on X, P_0 the total pressure at the column inlet, and P_{sat} the water vapor saturation pressure in air.

The droplet mass can be written as:

$$m_d = m_s(1 + X + Z) = \rho_d (4/3)\pi R^3 \tag{8}$$

where m_s is the mass of solute in a droplet, ρ_d is the droplet density (which is equal to the solution density ρ_{liq} before precipitation), and R its radius.

From relation (8), this latter can be written as:

$$R = R_0 \left(\frac{\rho_{liq,0}}{\rho_{liq}} \cdot \frac{1 + X}{1 + X_0}\right)^{1/3} \tag{9}$$

where R_0 and X_0 are the initial values of R and X.

From (9), a simple expression of droplet radius R_p at the onset of precipitation can be given:

$$R_p = R_0 \left(\frac{\rho_{liq,0}}{\rho_{liq}^{sat}} \cdot \frac{1 + X_{sat}}{1 + X_0}\right)^{1/3} \tag{10}$$

where X_{sat} and ρ_{liq}^{sat} are the values of X and of the droplet density at the solubility limit respectively.

Modeling of transport phenomena inside liquid droplets along the column height

Assuming that the temperature inside the droplets is uniform, momentum and mass transport (diffusion + convection) occurring inside the droplets during the pure evaporation stage can be described by the classical local equations whose variables are the radial liquid velocity in a droplet and the solute concentration in the droplet c_s (or w_s^{liq}) and using a 1D-spherical approach.[13]

The flux density of water evaporated at the droplet surface has been calculated from the 1D + 0D approach. The coupled resolution of the 1D + 0D system and of these latter 1D-spherical equations provides a consistent 1D + 1D approach. Note that the reduced mass fraction X in the 1D + 0D approach is no longer considered as a uniform parameter, but as an average value in the droplet, and that the water activity a_w must now be calculated as a function of w_w^{liq} and w_s^{liq} at the droplet interface, and not as a function of X anymore. The binary diffusion coefficient of water/solute can be calculated from the mean ionic activity coefficient of the solution given in Table 1.[24–26]

To solve these systems in coupled mode, all these equations were implemented in the same problem, where the first system (1D + 0D approach) was solved along one direction, and the second system (1D-spherical equations) along another direction. Thus, a two-dimensional grid was used. All these equations were implemented in the finite element solver FlexPDE,[28] which uses a modified Newton-Raphson iteration process and a mesh generator with automatic refinement.

Results and discussion

First, drying with an air flow rate of 4.7 m^3/h STP has been studied. As can be seen in Figure 1, the decrease of the radius of pure water droplets is faster than the decrease of the radius of water + solute droplets: evaporation is com-

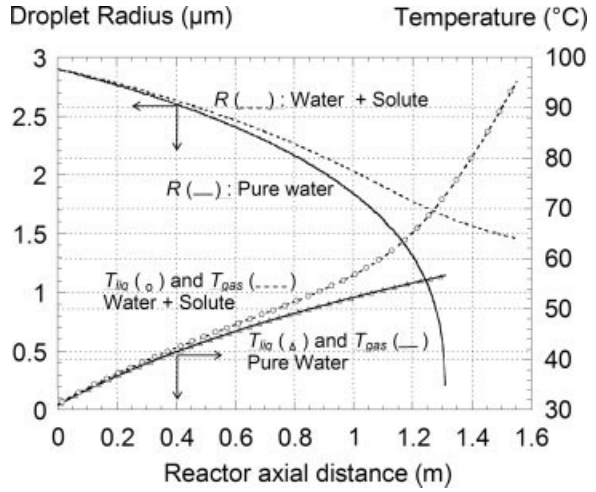

Figure 1. Variation of the droplet radius, gas and liquid temperatures along the reactor axis for pure water and (water + Y^{3+}/NO_3^-)—Fv_a = 4.7 m^3/h STP, Fv_w = 0.32 l/h STP, R_0 = 2.9 μm.

plete at a position of 1.31 m for pure water droplets whereas the solubility limit is reached at 1.55 m for water + solute droplets. This is due to the fact that in the latter case, the lower water activity involves a lower interfacial saturation pressure and therefore a lower evaporation rate. From these results, it can be deduced that the drying of the water + solute spray requires a higher amount of energy, about 18% more for the operating conditions tested.

In both cases, the temperature of the liquid phase remains equal to that of the gas phase as presented in Figure 1. This result is due to the high value of the heat transfer coefficient at the liquid/gas interface. For the pure water droplets, the final temperature was 56.7°C after total evaporation whereas it was 95.2°C for drying water + solute droplets at the onset of precipitation (in which a lot of water remains).

Whatever the air/water flow rate, the solute concentration in droplets increased from a value of 0.75 mol/l at the reactor inlet to 5.93 mol/l at the onset of precipitation. But no significant concentration gradient appeared along the droplet radius during the evaporation stage. This result is true for our whole range of operating parameters. Xiong and Kodas[14] came to the same conclusion for similar processing conditions. Note that no concentration gradient would have been obtained even if a critical supersaturation concentration (greater than the one predicted by the solubility limit law given in Table 2) had been considered.

Such a result can also be obtained estimating the ratio of the characteristic time of diffusion of the solute in liquid water to the total time of evaporation[12] (from 1D calculations, this latter varies between 25 and 60 s depending on the flow rates). In our range of operating parameters, this ratio remains lower than 5×10^{-4}, which is very low, meaning that solute concentration gradients might not appear. Our precise 1D-spherical model, which considered convection and a precise description of diffusion, confirmed this trend.

Likewise, we can estimate the ratio of the characteristic time of heat diffusion in the droplet to the total time of evaporation.[12] It is lower than the former by several orders of magnitude. The assumption of uniform temperature in droplets is therefore fully justified for our operating conditions.

The variation of the spray temperature along the column height for the various flow rates studied is given in Figure 2. Logically, for a given position in the column, the temperature decreases if the flow rate increases. The reactor height necessary for complete evaporation increases with the air/water flow rate. The total energy consumed during the evaporation stage is proportional to the air/solution flow rate and is equal to about 2520 kJ/l of solution for the evaporation stage (i.e. a total power of 700 W). The calculated temperature at the onset of precipitation was always equal to 95°C. The average temperatures measured in the flow 1.5 m after the column inlet are reported in Figure 2. Some measurements were also carried out at intermediate positions for the highest flow rate and appear to be well estimated by calculations.

Table 2. Expressions of the Droplet/Particle Porosity, Particle Radius, and Position of Air/Liquid Interface Inside Particles, for the Three Scenarios Considered in the Model of Precipitation

Porosity	Particle Radius	Position of Air/Liquid Interface
Case 1 $\varepsilon_f = 1 - \alpha \frac{\rho_{liq}^{sat}}{\rho_{cryst}}$	$R = R_p$	$r_{int} = r_{int,0}\left(\frac{X}{X_{sat}-Z_f}\right)^{1/3}$ with: $r_{int,0} = R_0\left(\frac{\rho_{liq,0}}{\rho_w} \cdot \frac{X_{sat}-Z_f}{1+X_0} \cdot \frac{1}{\varepsilon_f}\right)^{1/3}$
Case 2a $\varepsilon_f = 1 - \alpha \frac{\rho_{liq}^{sat}}{\rho_{cryst}}$	$R = R_p$	$r_{int} = R_p\left(\frac{X}{X_{sat}}\right)^{1/3}$
Case 2b 1st stage: $\varepsilon = \left(1 + \alpha \frac{\rho_{liq}^{sat}}{\rho_{cryst}} \cdot \left(\frac{X_{sat}}{X} - 1\right)\right)^{-1}$	$R = R_0\left(\frac{\rho_{liq,0}}{\rho_d} \cdot \frac{1+X+Z}{1+X_0}\right)^{1/3}$ with: $\rho_d = \varepsilon\rho_{liq}^{sat} + (1-\varepsilon)\,\rho_{cryst}$	$r_{int} = R$
2nd stage: $\varepsilon = \varepsilon_c\left(\frac{r}{R_c}\right)^{\beta}$	$R_c = R_0\left(\frac{\rho_{liq,0}}{\rho_d^c} \cdot \frac{1+X_c+Z_c}{1+X_0}\right)^{1/3}$ with: $X_c = X_{sat}\left(1 + \frac{1-\varepsilon_c}{\varepsilon_c} \cdot \frac{\rho_{cryst}}{\rho_{liq}^{sat}}\alpha^{-1}\right)^{-1}$	$r_{int} = R_c\left(\frac{X}{X_c}\right)^{1/(3+\beta)}$

With $\alpha = \left(\frac{1+Z_f}{1+X_{sat}}\right)$ and $\beta = \left(\frac{\rho_{cryst}}{\rho_{liq}^{sat}}\alpha^{-1} - 1\right)^{-1}$.

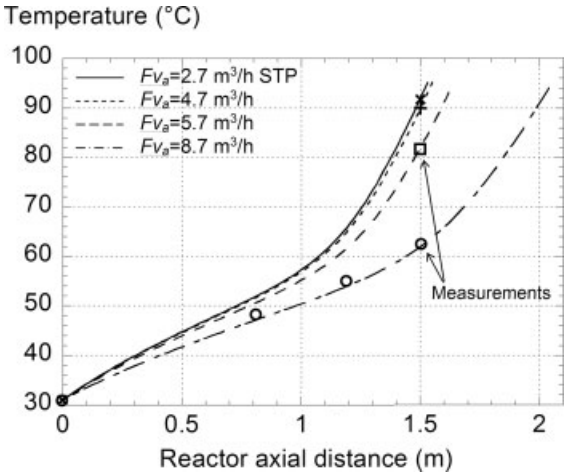

Figure 2. Variation of the spray temperature along the reactor axis for several air flow rates.

In all cases, the variation of droplet radius follows the classical D^2-law (i.e. the relationship between droplet surface change vs. residence time is linear).[27,29] As reported in Figure 3, the variations of the droplet radius and of the solute concentration in the droplets vs. temperature were the same whatever the initial flow rates. In particular, droplet radius and droplet concentration at the onset of precipitation were always the same: 1.46 μm and 5.93 mol/l, respectively. This can be explained by the fact that the initial solution flow rate was always proportional to the air flow rate and by the fact that the limiting step here is clearly heat transfer from reactor walls to the spray, not mass transfer at the air/water interface and/or inside the droplet. Actually, at a given position in the reactor, the local temperature determines the interfacial saturation pressure and therefore the total amount of evaporated water. Over our range of operating parameters, it can be deduced that the droplet radius and the uniform solute concentration depends only on the local temperature and not on the thermal history of the spray. We verified that this quasi-steady state of the evaporation process held true for a wide range of processing parameters.[4]

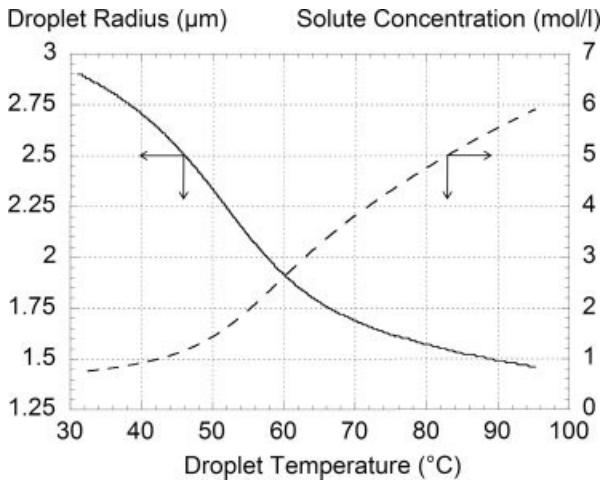

Figure 3. Variation of the droplet radius and of the solute concentration vs. droplet temperature.

Since saturation was always reached at 95°C and at 5.93 mol/l, X_{sat} and ρ_{liq}^{sat} always take the same values and therefore so does R_p given by relation (10).

Modeling of the Evaporation/Precipitation Step

Reaction of precipitation and properties of the precipitate

Once the solubility limit is reached somewhere in the liquid droplet, the solute locally begins to precipitate, following the reaction:

$$Y^{3+} + 3\ NO_3^- + n_w H_2O \rightarrow Y(NO_3)_3 \cdot n_w H_2O \qquad (R1)$$

The solid phase is then composed of hydrated yttrium nitrate molecules. The n_w weakly bound water molecules are evacuated only during the thermolysis step. Depending on the temperature, this number of water molecules n_w can be 6, 5, 4, or less, as shown in the binary diagram H_2O-$Y(NO_3)_3$ in Figure 4. This diagram was determined by Bouchet et al.[26] by both experiment and numerical simulation. The curve of solute mass fraction/temperature predicted by our model of the pure evaporation stage (for an air flow rate of 4.7 m^3/h STP) is reported in this figure.

At temperatures greater than about 40°C, the precipitate formed is a mixture of hexahydrate/pentahydrate or pentahydrate/tetrahydrate yttrium nitrate depending on temperature ranges and some water in excess remains liquid. In the present work, we considered the following simplified scheme:

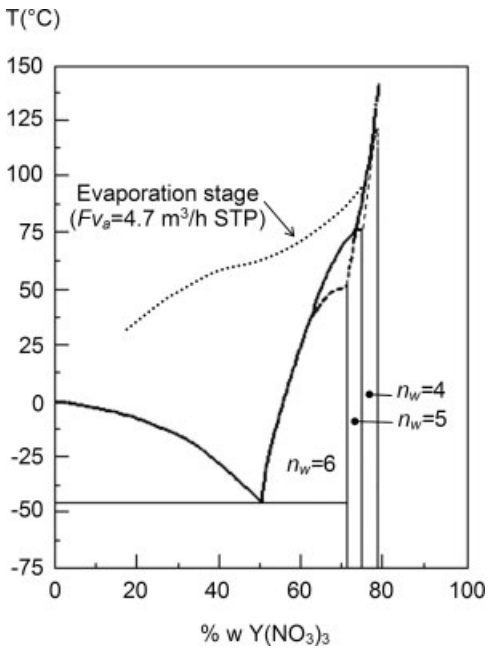

Figure 4. Binary diagram for the H_2O-$Y(NO_3)_3$ system[26]—domains of solid $Y(NO_3)_3 \cdot n_w H_2O$ indicated by the values of n_w.

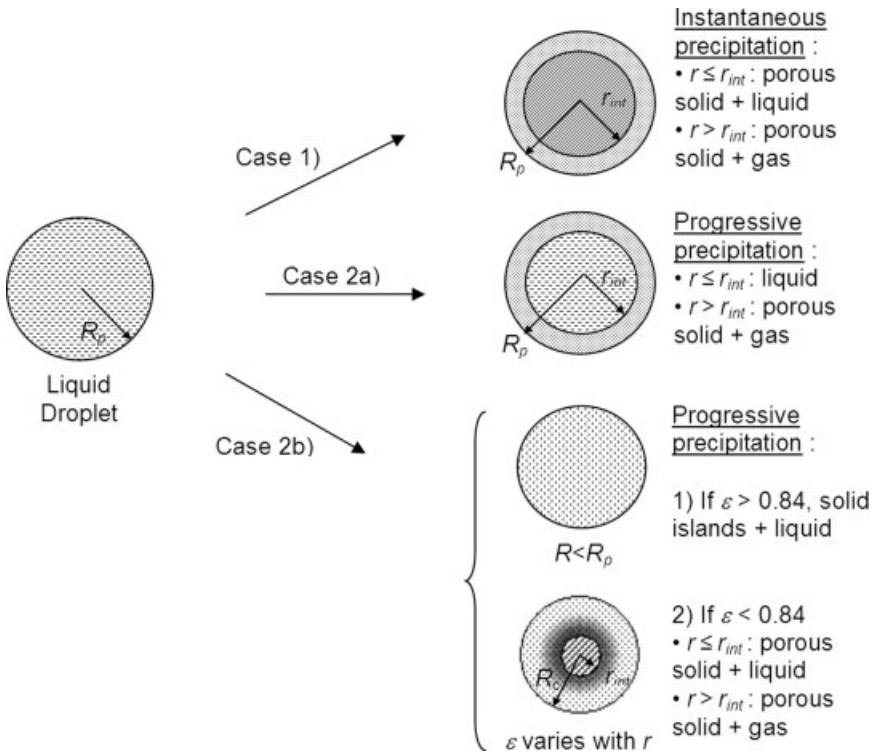

Figure 5. Schematic representation of the various cases of precipitation/evaporation.

• formation of the $Y(NO_3)_3{\cdot}6H2O$ precipitate for a solution temperature $T_{liq} < 74°C$,

• formation of the $Y(NO_3)_3{\cdot}5H2O$ precipitate for $74°C < T_{liq} < 104°C$,

• formation of the $Y(NO_3)_3{\cdot}4H2O$ precipitate for $T_{liq} > 104°C$.

Note that these limit temperatures were determined from the binary diagram: the first and the second ones corresponding to the temperatures at which the solution at the onset of precipitation contains exactly 6 and 5 moles of H_2O respectively for 1 mole of $Y(NO_3)_3$.

In the general case, when the solution begins to precipitate, there is an excess of water molecules. They can stay in a liquid state in the droplet/particles and/or evaporate. This is why we have to consider an evaporation/precipitation stage; we intend to describe it with the following model.

The density ρ_{cryst} of $Y(NO_3)_3{\cdot}6H_2O$ is 2680 kg/m^3. From the enthalpy of formation of the reactive and product species,[30] a crystallization enthalpy ΔH equal to 34.2 kJ/mol was determined for $n_w = 6$. Since these last two parameters were not found for the other hydrates, we took the same values.

Description of the evaporation/precipitation model

Since it is established that no concentration gradient occurs during the evaporation stage, it is now possible to model the evaporation/precipitation stage still using Eqs. 3–6 of the 1D + 0D system, but introducing the following new parameter Z:

$$Z = w_w^{cryst}\left(w_s^{liq} + w_s^{cryst}\right)^{-1} \tag{11}$$

where a distinction between the mass fraction of water in the solid precipitate w_w^{crist} and that in the solution w_w^{liq} must be considered.

Once the precipitation is complete and the free liquid water has completely disappeared, the final value of Z is:

$$Z_f = n_w M_w M_s^{-1} \tag{12}$$

where M_w and M_s are the molar weights of water and of the solute respectively.

If the air/solution interface is exactly at the surface of the droplet/particle, the parameter D_v in Eq. 4 is equal to the binary diffusion coefficient of air/water vapor. But if the air/solution interface is inside the droplet/particle, due to the formation of a porous crust, the law of evaporation must be modified according to Nesic and Vodnik[31] and the parameter D_v in Eq. 4 must be replaced by the following apparent diffusion coefficient D_v^p:

$$D_v^p = D_v\left(1 + \frac{D_v}{D_{cr}} \cdot \frac{R - r_{int}}{r_{int}}\right)^{-1} \tag{13}$$

where r_{int} is the position of the air/solution interface along the droplet/particle radius and D_{cr} is the diffusivity of vapor through the precipitated layer. This latter parameter can be expressed as a function of the crust porosity ε:

$$D_{cr} = \frac{\varepsilon}{\tau} D_v \tag{14}$$

Finally, assuming the tortuosity τ equal to 1, expression (13) becomes:

$$D_v^p = D_v\left(1 + \frac{1}{\varepsilon} \cdot \frac{R - r_{int}}{r_{int}}\right)^{-1} \tag{15}$$

Two scenarios of precipitation were then considered, as detailed below and illustrated in Figure 5.

Case 1: Instantaneous Precipitation. The droplet radius is not affected by the initial solute precipitation and remains equal to the droplet radius at the onset of precipitation R_p. Since the density of the precipitate ρ_{cryst} is greater than the density of the saturated solution ρ_{liq}^{sat}, the particle obtained must be porous. Water in excess remains liquid and fills part of the porosity. Because of the still increasing temperature, this liquid water will continue to evaporate. Thus, the water vapor will diffuse through the porous medium toward the surface until the particle is completely dry.

The reduced mass fraction Z of water present as hydrate in the solid precipitate becomes instantaneously equal to Z_f given by relation (12), and the final particle porosity ε_f, assumed uniformly distributed, is given in Table 2. Some pure liquid water remains in the pores, its reduced mass fraction corresponds to the difference between X_{sat} and Z_f.

Because of the difference in densities of the saturated solution ρ_{liq}^{sat} on one hand, and of the precipitate ρ_{cryst} and of pure water ρ_w on the other hand, it appears that the liquid water does not fill all the porosity. Thus, some air must necessarily penetrate into the particle. We considered here the most unfavorable case (in terms of facility of water evaporation) for which all the water in excess completely fills the pores toward the particle's center while air fills the pores toward the particle's border. Therefore, the position of the air/water interface along the particle radius just after precipitation corresponds to $r_{int,0}$ in Table 2. As liquid water evaporates through the crust, the current position r_{int} of air/water interface decreases along the particle radius, as given in Table 2.

Case 2: Progressive Precipitation. The temperature increase along the column leads to continuous water evaporation. As soon as the solubility limit is exceeded somewhere in the solution, precipitation occurs and stops when the solubility limit is no longer exceeded in the liquid phase. Therefore, we have:

$$\frac{Z}{Z_f} + \frac{X}{X_{sat}} = 1 \tag{16}$$

Two subcases must now be considered:

- 2a, precipitation is much more rapid than species diffusion;
- 2b, species diffusion is much more rapid than precipitation.

In subcase 2a, as soon as a few water molecules have evaporated at the air/solution interface, the solubility limit is locally exceeded and a fraction of the solution precipitates. As water evaporation initially occurs at the droplet surface, precipitation will first concern the outer part of the droplet and near the central particle part, the solution remains unchanged. As the evaporation process occurs, the air/solution interface moves progressively from the particle surface toward the particle center and a front of precipitation follows it. In this case, clearly the particle radius does not change and remains equal to R_p.

Actually, the mathematical description of this problem is similar to that of the instantaneous precipitation case. Once the precipitation front has passed, the final porosity ε_f is the same as previously. The current position of the air/solution interface is given in Table 2.

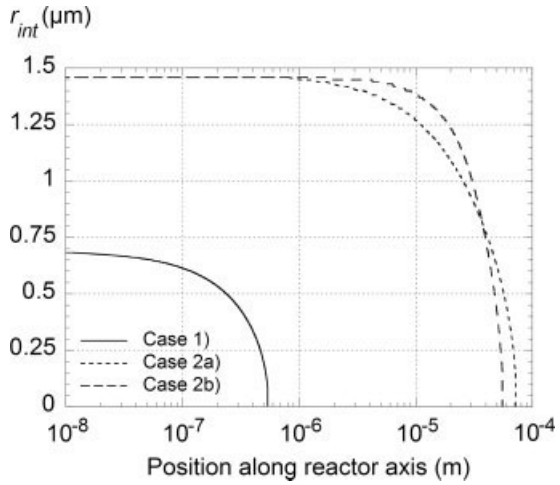

Figure 6. Position of the air/liquid interface radius along the column axis for the three scenarios of precipitation—Fv_a = 4.7 m³/h STP.

In the scenario 2b, as soon as a few water molecules evaporate at the air/solution interface, species diffuse quickly and we assume that no significant concentration gradient is created. Thus, the solubility limit is exceeded everywhere in the solution at the same time and a fraction of the solution precipitates. As the evaporation process occurs, solid islands grow everywhere throughout the droplet. As long as a coherent porous medium is not formed, the droplet radius continues to decrease and the air/solution interface remains at the surface. The expressions for the droplet radius and the porosity during this first stage are reported in Table 2.

According to Jayanthi et al.[12] and Zallen,[32] as soon as the porosity in the droplet becomes lower than the critical value ε_c of 0.84, a coherent porous medium is formed. At this time, the particle radius R takes the value R_c and X takes the value X_c given in Table 2.

Then, the particle radius remains equal to R_c, the evaporation process goes on, and the position of the air/solution interface is now given by the expression of r_{int} reported in Table 2. The porosity inside the liquid/solid area ($r < r_{int}$) is equal to $\varepsilon(r_{int})$ and is therefore independent of the position along the droplet radius whereas the final porosity outside the liquid/solid area ($r > r_{int}$) varies as a function of the position along the droplet radius and is equal to $\varepsilon(r)$ (Table 2). Hence, at the end of the evaporation/precipitation process, a porosity gradient is obtained between the particle surface (where $\varepsilon = \varepsilon_c$) and the particle center (where $\varepsilon = 0$). For the calculation of coefficient D_v^p (15), a porosity equal to $\varepsilon(r_{int})$ was considered and no percolation threshold was taken into account (actually, as porosity becomes very small, lower than 0.05 for regular or random lattices of spheres,[33,34] pores tend to disconnect and tortuosity becomes infinite).

Results and discussion

In all cases, from our simplified scheme, the precipitate formed is $Y(NO_3)_3 \cdot 5H_2O$ (most probably a mixture of two of

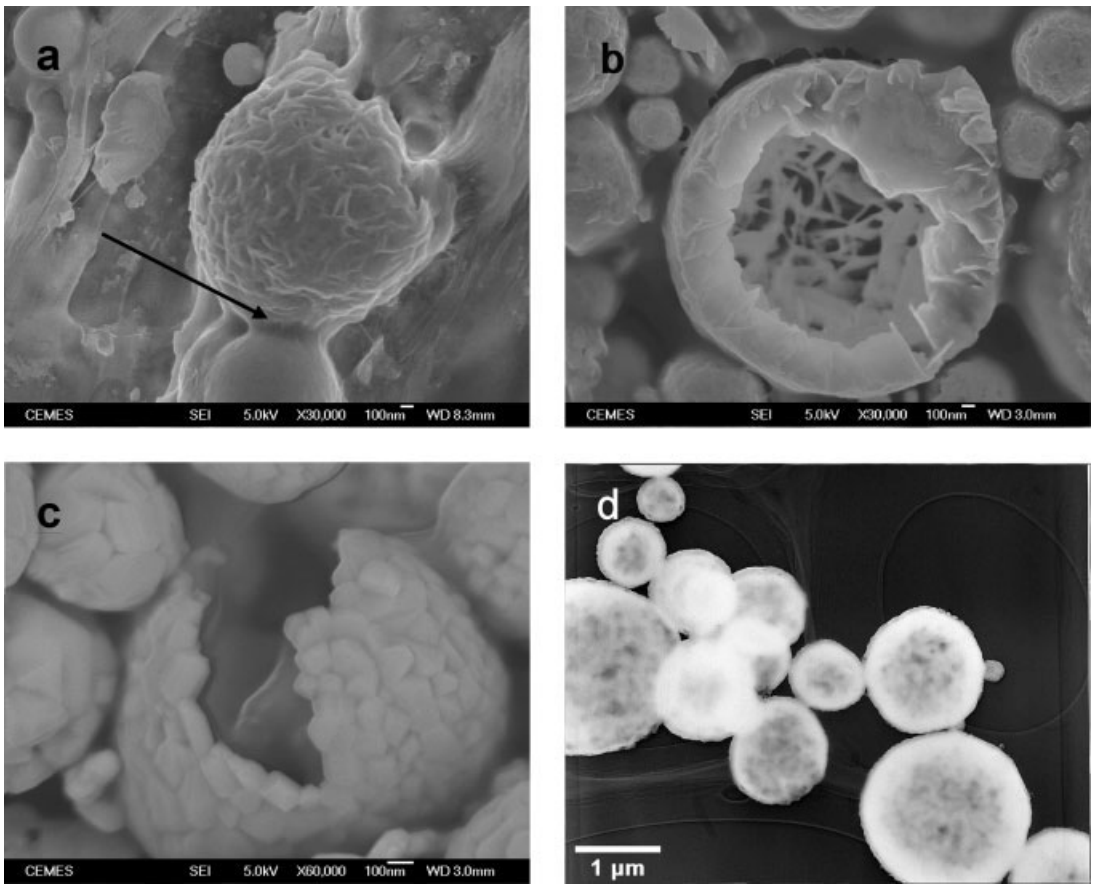

Figure 7. (a–c) SEM images of particles collected at various stages of the process.

(a) after drying and first step of thermolysis (120°C); (b) broken sphere ($YO(NO_3)$ and $Y(NO_3)_3$) after thermolysis at 400°C; (c) broken Y_2O_3 sphere after thermolysis at 700°C and postannealing at 1400°C; (d) TEM image of Y_2O_3 after thermolysis at 700°C and postannealing at 1200°C.

the three hydrates in reality). For scenarios 1 and 2a, droplet/particle radii remain equal to R_p (1.46 μm). The evolution of the water/gas interface r_{int} along the reactor axis, for an air flow rate of 4.7 m^3/h STP and for the three scenarios considered, is shown in Figure 6.

For the case 1, whatever the air/flow rate, evaporation of water in excess in the precipitated particle is extremely rapid: it is complete over a distance of less than 1 μm corresponding to a residence time shorter than 13 μs. This is due to the fact that the water activity becomes instantaneously equal to 1 in this case. The final porosity is uniform and equal to 0.2, which is clearly lower than the critical porosity of 0.84. Thus, the final particle is relatively compact.

For scenario 2a, evaporation of water in excess and simultaneous precipitation occurs over a distance less than 0.1 mm and a residence time shorter than 1.6 ms. In this case, the second stage of drying is therefore about 100 times longer than in case 1. But the final porosity is also uniform and equal to 0.2.

Finally, for case 2b, water evaporation and simultaneous precipitation occur over a distance of less than 0.08 mm and a residence time shorter than 1.1 ms. The final porosity varies from zero at the particle center to 0.84 at its surface and the final radius is equal to 1.44 μm.

In all cases, whatever the assumptions made and for the tested operating conditions, the second stage of drying is very brief and all water in excess is evaporated. The particles obtained are relatively compact and the porosities always lower than ε_c. It is then likely that the hollowness of the particles does not result from this step.

Unfortunately, particles can not be really chemically or physically characterized just after this step because their constitutive materials, hydrates of yttrium nitrates ($Y(NO_3)_3 \cdot n_wH_2O$), are deliquescent and therefore very unstable.[35] Nevertheless, it has been possible to collect few particles on a fibrous substrate (filter) put at the end of the drying column (≈120°C). As soon as the experiment has ended, a small sheet of the filter has been cut, put in a desiccator and then observed by SEM as quickly as possible (a few minutes). In Figure 7a, we can observe clearly (see the arrow) two spheres partially merged showing the deliquescent nature of this solid and/or the existence of a melting stage as detailed below.

Considerations About the Thermolysis Stage

The exact morphology of the formed particles could only be analyzed from synthesis temperatures of about 400°C: at this point, they are hollow. We will then search if the origin of this phenomenon proceeds from the thermolysis stage at temperatures higher than 95°C.

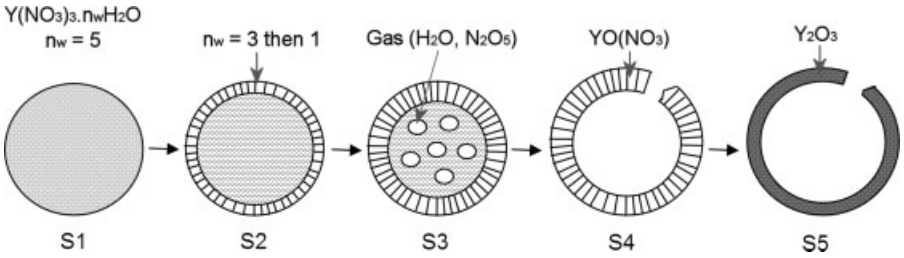

Figure 8. Schematic representation of the droplet morphology evolution during the thermolysis step.

Above 95°C, the thermolysis of hydrated yttrium nitrates goes on. Odent and Autrusseau-Duperray[36] investigated the decomposition of $Y(NO_3)_3.5H_2O$ by TGA, TDA, chemical analyses and XRD. They identified successively the hydrates at $3H_2O$ (formed at 80°C, fused at 115°C) and $1H_2O$ (formed at 170°C, fused at 232°C), the anhydrous nitrate $Y(NO_3)_3$ (formed at 290°C), the oxide nitrate $YO(NO_3)$ (formed at 350°C), then the sesquioxide Y_2O_3 formed in two steps at 450 and 510°C. These observations were corroborated by several investigators, for instance Bouchet et al.[26] (a hydrate at $4H_2O$ was also reported) and Pelloquin et al.[37]

For our processing conditions, all transitions from $Y(NO_3)_3$ $5H_2O$ to Y_2O_3 are completed within 25–85 s in the decomposition zone (according to the air flow rate chosen), that is much faster than the measurement conditions used in the preceding references. We performed some characterizations of the powders in order to get information on the chemical reactions that occurred in real operating conditions. The air flow rate was of 4.7 m^3/h STP and the outer wall temperature of the drying zone was fixed at 225°C. The outer wall temperature of the decomposition/densification zone was fixed at 400 and 700°C for synthesis No. 1 and No. 2, respectively.

Synthesis No. 1: XRD exhibits an important diffusion background due to amorphous phase. Some diffraction peaks are nevertheless observed. Some of them correspond to the oxide nitrate (by comparison with Pelloquin et al.[37]), others are tentatively assigned to hydrated phases. By thermal analysis (GTA/DTA) a weight loss associated to an endothermic peak at 170°C is observed (the $Y(NO_3)_3$ $3H_2O$ to $Y(NO_3)_3.1H_2O$ decomposition—Odent and Autrusseau-Duperray[36]). At higher temperatures, thermal events are observed: at 350°C, formation of $YO(NO)_3$ (see Odent and Autrusseau-Duperray[36]), at 450 and 510°C, transformation of $YO(NO)_3$ in Y_2O_3 (see Odent and Autrusseau-Duperray[36]).

Synthesis No. 2: XRD exhibits only the C-Y_2O_3 crystallized phase (with broad diffraction lines) superposed on a diffusion background. The thermal analysis reveals residual water and nitrate.

The morphologies of the particles observed by SEM were very much the same for both syntheses: when broken spheres are found, they consist of a hollow center and of a shell made of crystalline platelets (see Figure 7b). The radial character of the growth direction strongly suggests that the crystallization phenomenon starts from the surface and then progresses to the core. The complete crystallization of C-Y_2O_3 is achieved only after postsynthesis annealing at higher temperatures (1200–1400°C). The crystallite platelets have transformed into isotropic crystals and the core-shell configuration is maintained (see Figure 7c). Smaller fragments can also be observed, but most of the particles are spheres or broken spheres. Even the smallest particles are hollow, this can be deduced from TEM images since there is more contrast at the periphery of the particles than in their center, as shown in Figure 7d.

The phenomena occurring during this step are particularly complex and we do not intend to model them. However, interesting information is available which allows a qualitative description of the thermolysis stage.

At the end of the pure evaporation stage, the temperature is about 95°C, the droplets precipitate, and the water in excess is quickly evacuated. Dry particles of $Y(NO_3)_3{\cdot}5H_2O$ are obtained, as illustrated in Figure 8-S1.

What occurs then? The temperature continues to increase, and, as can be seen in the phase diagram (Figure 4), the material tends to liquefy again. But as soon as a microscopic part of the particle liquefies, the water in excess evaporates and diffuses like in the previous stage. Therefore, while the temperature continues to increase, the yttrium nitrate progressively loses its hydrates. Extrapolating the interfacial saturation pressure of water in a $Y(NO_3)_3$ solution, we have estimated the boiling temperature as equal to about 160°C. From this temperature and above, the hydrated nitrate looses progressively water in the vapor state, gaseous NO_2 starting to evacuate at 200°C. We can assume that the evacuation of vapor water is easier near the particle surface, and therefore a crust of low hydrated yttrium nitrate is formed whereas at the particle center, it is more hydrated and maybe liquid (Figure 8-S2). Whereas the dehydration front moves progressively from the surface to the core, a pressure gradient resulting from the production of gaseous species appears between the particle center and the particle surface and comes greater. Moreover, the liquefaction of the low hydrated yttrium nitrates at their points of fusion tends to decrease the permeability of the crust. Because of these phenomena, particle inflation can occur, and yttrium based material, which is rather viscous as long as it contains water molecules, tends to be moved from the particle center toward the surface. The direct consequence is the formation of hollow swollen particles, which can be broken if the permeability of the crust is too low and the gas pressure inside the particles too high (Figure 8-S3,S4). Finally, from about 450 to 1200°C, the oxide nitrate is progressively transformed into a pure oxide. The shell thickness is then reduced as the density of the material increases (Figure 8-S5). It must be emphasized that in this particular system, most of the resulting particles are spherical and did not explode into particle fragments as may happen for other metal nitrates.

Note that between the onset of precipitation and the end of the process, about 60% of the particle mass is lost under gaseous form (water, NO_2 and N_2O_5). If the remaining mass (Y_2O_3) were uniformly distributed all over the particle (considering a constant radius), the final porosity would be about of 0.64.

Conclusion

SP is an efficient process to synthesize europium doped yttrium oxide Y_2O_3:Eu micronic particles of interest for luminescent applications. However, particles are collected under the form of hollow spheres: this morphology may be inappropriate for some applications.

It was to make progress in understanding the process that a modeling study of the drying step was first performed at the scales of the column and of the droplet. The pure evaporation stage then the stage of evaporation/precipitation was considered. Different scenarios of precipitation were proposed including instantaneous precipitation and progressive precipitation in the diffusion regime then in the phase change regime.

Among the numerous results obtained, it was in particular demonstrated that the temperature of the liquid phase is always equal to that of the gas phase. At the onset of precipitation, for the whole range of conditions tested, the particle radius was always equal to 1.46 μm and the onset temperature 95°C. For the operating range tested, the evolution of the droplet radius was only found to depend on the local temperature, not on the thermal history of the spray. For the simulated conditions, no concentration gradient appeared inside droplets during the evaporation stage.

For all the tested scenarios, the evaporation/precipitation stage proved to be very rapid, leading to complete evaporation of the water and to the formation of compact particles thought to be formed of a coherent porous medium of $Y(NO_3)_3{\cdot}5H_2O$.

Finally, the phenomena occurring during the thermolysis step for temperatures between 95 and 400°C were described on the basis of qualitative theoretical considerations and experimental data. This revealed that a partial liquefaction of the hydrated yttrium nitrate occurs with a concomitant release of gaseous water and N_2O_5. A crust of low hydrated yttrium nitrate probably appears, followed by particle inflation, leading to the formation of hollow open or broken particles.

Now one may ask: what must be done to avoid hollow particles formation? The answer appears to be the following: avoiding precursors for which intermediate viscous or molten phases appear during the thermolysis step to yield a crust with low permeability and release abundant gaseous species. Using a reticulating agent such as polyethylene glycol was found to be a good solution probably because it enhances the consistency of the intermediate phases, prevent the formation of low permeable shells and thus prevent particle inflation during the thermolysis stage.

Notation

a_w = water activity
C_p = specific heat (J/kg K)
C_{pw}^{vap} = specific heat of water vapor (J/kg K)
D_{cr} = diffusivity of vapor through the precipitate layer (m^2/s)
D_v = binary diffusion coefficient of air/water vapor (m^2/s)
D_v^p = apparent diffusion coefficient of water vapor through the droplet (m^2/s)
F = mass flow rate (kg/s)
Fv = volume flow rate (m^3/h STP)
h_{vap} = vaporization enthalpy of water (J/kg)
m_d = droplet mass (kg)
m_s = mass of solute in droplet (kg)
M = molar mass (kg/mol)
n_w = number of water molecules present as hydrates in an yttrium nitrate molecule
P_0 = ambient pressure (Pa)
P_{sat} = saturation pressure of water vapor in air (Pa)
q = heat flux density at the inner wall (W/m^2)
r = radial coordinate inside droplet or particle (m)
r_{int} = position of air/liquid interface along droplet radius (m)
R = droplet radius (m)
R_p = droplet radius at the onset of precipitation (m)
R_c = reactor radius (m)
S = solubility (g/100 g of water)
T = temperature (K)
T_{wall} = inner wall temperature (K)
v_z = gas velocity along reactor axis (m/s)
w_a, w_w^{vap} = mass fractions of air/water vapor in gas
w_s^{cryst} = mass fractions of solid $Y(NO_3)_3$ in droplet
w_w^{cryst} = mass fraction of water present as hydrates of yttrium nitrate in droplet
w_w^{liq} = mass fraction of liquid water in droplet
w_s^{liq} = mass fractions of $Y(NO_3)_3$ in droplet
X, Y, Z = relative mass fractions defined at (2) and at (11)
X_c, Z_c = relative mass fractions defined at (2) at the critical porosity
Y_{int} = Y defined at (7)
Z_f = final value of Z
z = axial coordinate

Greek letters

ε = porosity of the crust
ε_c = critical porosity
ε_f = final porosity
$\gamma_\pm$ = mean ionic activity coefficient
κ = constant defined at (1) (W/m^2 K)
λ = thermal conductivity (W/m K)
ΔH = crystallization enthalpy of the solute (J/kg)
ρ = density (kg/m)
τ = tortuosity of the crust

Subscripts

0 = initial value
a = air
cryst = precipitate
d = droplet
gas = gas
int = at the gas/liquid interface
liq = liquid
s = solute
sat = in the saturated solution (i.e. at the solubility limit)
w = water

Acknowledgments

The authors gratefully acknowledge Prof. J. P. Couderc for his valuable contribution. This work has been supported by the French Ministère de la Recherche (RNMP/POSUMIC) and by the Midi-Pyrénées Regional Council. The authors wish to thank the society RHODIA which supplied the yttrium nitrate solution for these experiments.

Literature Cited

1. Gurav A, Kodas T, Pluym T, Xiong Y. Aerosol processing of materials. *Aerosol Sci Technol.* 1993;19:411–452.

2. Pratsinis SE, Vemury S. Particle formation in gases. *Powder Technol*. 1996;88:267–273.
3. Joffin N. Synthèse par pyrolyse d'aérosol et caractérisation de luminophores: Y_2O_3:Eu et Zn_2SiO_4:Mn pour application dans les panneaux à plasma. PhD Thesis, Institut National Polytechnique Toulouse, France, 2004.
4. Reuge N, Dexpert-Ghys J, Verelst M, Caussat B. Y_2O_3 micronic particles synthesised by spray pyrolysis: global modelling and optimisation of the evaporation stage. *Chem Eng Process*. In press.
5. Lyons SW, Ortega J, Wang LM, Kodas TT. Multicomponent ceramic powder generation by spray pyrolysis. *Mater Res Soc Symp Proc*. 1992;271:907–917.
6. Lenggoro IW, Hata T, Iskandar F. An experimental and modelling investigation of particle production by spray pyrolysis using a laminar flow aerosol reactor. *J Mater Res*. 2000;15:733–743.
7. Joffin N, Dexpert-Ghys J, Verelst M, Baret G, Garcia A. The influence of microstructure on luminescent properties of Y_2O_3: Eu prepared by spray pyrolysis. *J Lumin*. 2005;113:249–257.
8. Joffin N, Caillier B, Dexpert-Ghys J, Verelst M, Baret G, Garcia A, Guillot P, Galy J, Mauricot R, Schamm S. Elaboration by spray pyrolysis and characterization in the VUV range of phosphor particles with spherical shape and micronic size. *J Phys D*. 2005;38:3261–3268.
9. Sohn JR, Kang YC, Park HD. Morphological control of Y_2O_3:Eu phosphor particles by adding polymeric precursors in spray pyrolysis. *Jpn J Appl Phys*. 2002;41:3006–3009.
10. Roh HS, Kang YC, Park HD, Park SB. Y_2O_3:Eu phosphor particles prepared by spray pyrolysis from a solution containing citric acid and polyethylene glycol. *Appl Phys A*. 2003;76:241–245.
11. Messing GL, Zhang S-C, Jayanthi GV. Ceramic powder synthesis by spray pyrolysis. *J Am Ceram Soc*. 1993;76:2707–2726.
12. Jayanthi GV, Zhang SC, Messing GL. Modeling of solid particle formation during solution aerosol thermolysis—the evaporation stage. *Aerosol Sci Technol*. 1993;19:478–490.
13. Yu H-F, Liao W-H. Evaporation of solution droplets in spray pyrolysis. *Int J Heat Mass Transfer*. 1998;41:993–1001.
14. Xiong Y, Kodas TT. Droplet evaporation and solute precipitation during spray pyrolysis. *J Aerosol Sci*. 1993;24:893–908.
15. Charlesworth DH Jr, Marshall WR. Evaporation from drops containing dissolved solids. *J AIChE*. 1960;6:9–23.
16. Lin J-C, Gentry JW. Spray drying drop morphology: experimental study. *Aerosol Sci Technol*. 2003;37:15–32.
17. Lin J-C, Gentry JW. Modeling of particle formation by spray drying process. *J Aerosol Sci*. 1997;28 (Suppl. 1):S477–S478.
18. Lin J-C, Gentry JW. Spray drying droplet morphology: theorical model. *J Aerosol Sci*. 1999;30 (Suppl. 1):S545–S546.
19. Lin J-C, Gentry JW. Spray drying droplet morphology: formation of shell. *J Aerosol Sci*. 2000;31 (Suppl. 1):S797–S798.
20. Reuge N, Caussat B. A dimensionless study of the evaporation and drying stages in spray pyrolysis. *Comput Chem Eng*. 2007;31:1088–1099.
21. Ronda CR. Recent achievements in research on phosphors for lamps and displays. *J Lumin*. 1997;72–74:49–54.
22. Kang YC, Park SB, Lenggoro IW, Okuyama K. Preparation of non-aggregated Y_2O_3:Eu phosphor particles by spray pyrolysis method. *J Mater Res*. 1999;14:2611–2615.
23. Rard JA. Solubility determinations by the isopiestic method and application to aqueous lanthanide nitrates at 25°C. *J Solution Chem*. 1985;14:457–471.
24. Reid RC, Prausnitz JM, Sherwood TK. *The Properties of Gases and Liquid, 3rd ed*. New York: McGraw Hill, 1977.
25. Dean JA. *Langes Handbook of Chemistry, 13th ed*. New York: McGraw Hill, 1985.
26. Bouchet R, Tenu R, Counioux JJ. Etude expérimentale et modélisation des équilibres solide-liquide des binaires eau-nitrate d'yttrium, de baryum, de cuivre. Partie 1. Les binaires H_2O-$Ba(NO_3)_2$ et H_2O-$Y(NO_3)_3$. *Thermochim Acta*. 1994;241:229–246.
27. Ranz WE Jr, Marshall WR. Evaporation from drops: part I and part II. *Chem Eng Prog*. 1952;48:141–146, 173–180.
28. www.pdesolutions.com.
29. Schlünder EU. Temperature und masseänderung verdunstander tropfen aus reinen flüssigkeiten und wässrigen salzlosungen. *Int J Heat Mass Transfer*. 1964;7:49–73.
30. Perachon G, Thourey J, Mathurin D. Enthalpies de formation du nitrate d'yttrium hexahydraté et de l'ion Y^{3+}. *Thermochim Acta*. 1977;18:229–234.
31. Nesic S, Vodnik J. Kinetics of droplet evaporation. *Chem Eng Sci*. 1991;46:527–537.
32. Zallen R. *The Physics of Amorphous Solids*. New York: Wiley-Interscience, 1983.
33. Roberts J, Schwartz L. Grain consolidation and electrical conductivity in porous media. *Phys Rev B*. 1985;31:5990–5997.
34. Hilfer R. Transport and relaxation phenomena in porous media. *Adv Chem Phys*. 1996;XCII:299–424.
35. Yost DM, Russel JH, Garner CS. *The Rare Earth Elements and their Compounds*. New York: Wiley, 1950:58–59.
36. Odent G, Autrusseau-Duperray M-H. Thermolyse du pentahydrate du nitrate d'yttrium. *Revue Chimie Minérale*. 1976;13:196–206.
37. Pelloquin D, Louër M, Louër D. Powder diffraction studies in the $YONO_3$-Y_2O_3 system. *J Solid State Chem*. 1994;112:182–188.